Simulating time harmonic flows with the lattice Boltzmann method

Lilit Axner,* Alfons G. Hoekstra,† and Peter M. A. Sloot‡
Section Computational Science, Laboratory for Computing, System Architecture and Programming, Faculty of Science, University of Amsterdam, Kruislaan 403, Amsterdam 1098 SJ, The Netherlands
(Received 18 August 2006; published 27 March 2007)

We simulate time harmonic flows by the lattice Boltzmann method. We propose a general scheme to choose simulation parameters, under the constraints of fixed Reynolds and Womersley numbers, and with a specified simulation error. Under these constraints parameters are chosen to minimize the execution time. Numerical stability is studied in a range of Reynolds and Womersley numbers. As an example of time harmonic flow simulations, results of blood flow in a human abdominal aorta are presented.

DOI: 10.1103/PhysRevE.75.036709 PACS number(s): 47.11.−j, 02.70.−c, 47.15.−x, 47.63.−b

I. INTRODUCTION

The lattice Boltzmann method (LBM) has attracted much attention and now is a well recognized method in computational fluid dynamics [1,2]. It is widely used in simulations of fluid flows in complex geometries such as fluid flow in porous media, e.g., [3–5], or time harmonic blood flow, e.g., [6–10]. However, the LBM is hampered by slow convergence [11–13], caused by the demand of low Mach number (Ma) (to suppress compressibility error) and the satisfaction of a Courant-Friedrich-Levy condition for numerical stability. In order to meet these constraints the number of time steps for reaching steady state needs to be large, and so is the execution time. For this reason we must carefully choose simulation parameters that, given the flow properties and target simulation error, minimize the execution time. We call this the constraint optimization problem for LBM simulations.

In this paper we propose a solution to the constraint optimization problem for time harmonic flows. For validation of the constraint optimization scheme we compare results of time harmonic flow simulations with analytical Womersley solutions [14]. We also perform stability analysis for a range of Reynolds (Re) and Womersley (α) numbers.

In Sec. II we give a short description of the LBM, in Sec. III we describe the constraint optimization scheme, in Sec. IV we discuss the stability of the LBM for time harmonic flows, and in Sec. V we use our results to simulate harmonic blood flow in the lower abdominal aorta. In Sec. VI we draw our conclusions.

II. LATTICE BOLTZMANN METHOD

The lattice Boltzmann method is based on the discrete velocity Boltzmann equation. In our simulations we use the lattice Bhatnagar-Gross-Krook model [15,16] (all the parameters are in lattice units and we assume $\delta x=\delta t=1$):

$$f_i(\boldsymbol{x}+\boldsymbol{e}_i,t+1)-f_i(\boldsymbol{x},t)=-\frac{1}{\tau}[f_i(\boldsymbol{x},t)-f_i^{(eq)}(\boldsymbol{x},t)] \quad (1)$$

with $\boldsymbol{e}_i$ the finite set of discrete velocities, τ the dimensionless relaxation parameter, $f_i(\boldsymbol{x},t)$ the density distribution function, and $f_i^{(eq)}(\boldsymbol{x},t)$ the equilibrium distribution defined by

$$f_i^{(eq)}=\rho w_i\left(1+\frac{\boldsymbol{e}_i\cdot\boldsymbol{u}}{c_s^{\,2}}+\frac{(\boldsymbol{e}_i\cdot\boldsymbol{u})^2}{2c_s^{\,4}}+\frac{\boldsymbol{u}\cdot\boldsymbol{u}}{2c_s^{\,2}}\right). \quad (2)$$

Here w_i is a weighting factor, $c_s=1/\sqrt{3}$ the speed of sound, ρ the hydrodynamic density determined by

$$\rho=\sum_i f_i=\sum_i f_i^{(eq)}, \quad (3)$$

and $\boldsymbol{u}$ the macroscopic velocity determined by

$$\rho\boldsymbol{u}=\sum_i \boldsymbol{e}_i f_i=\sum_i \boldsymbol{e}_i f_i^{(eq)}. \quad (4)$$

The viscosity ν of the fluid is determined by

$$\nu=\frac{1}{2}\frac{1}{3}\left(\tau-\frac{1}{2}\right). \quad (5)$$

We apply the three dimensional 19-velocity (D3Q19) model [16] for time harmonic flows [7]. The fluid flow is quasi-incompressible and all simulations in this paper (except those in Sec. V) are performed on a straight circular tube with rigid walls. On the walls we use Bouzidi boundary conditions (BBCs) [17]. For the experiments on the straight tube we use periodic inlet and outlet boundary conditions and the flow was driven by a time harmonic body force [6]. As we confirmed earlier for time harmonic flows [18] BBCs are more stable and accurate than the bounce-back on links boundary condition, especially for high Ma numbers. For the simulations we use a highly efficient parallel code [19].

We define an average simulation error ($\tilde{E}$) as

*Electronic address: labraham@science.uva.nl
†Electronic address: alfons@science.uva.nl
‡Electronic address: sloot@science.uva.nl

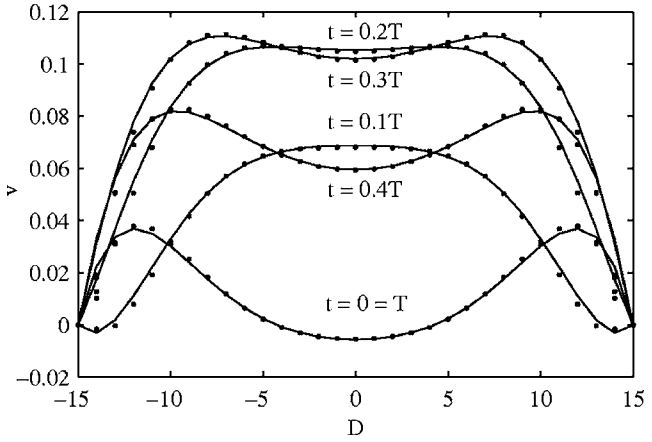

FIG. 1. Comparison of simulated velocity profile (dots) with analytical Womersley solution (solid line) for the tube with diameter $D=30$, Re=10, $\alpha=6$.

$$\tilde{E} = \frac{1}{T}\sum_t \frac{\sum_x |\boldsymbol{u}_{th}(\boldsymbol{x},t) - \boldsymbol{u}_{lb}(\boldsymbol{x},t)|}{\sum_x |\boldsymbol{u}_{th}(\boldsymbol{x},t)|}, \tag{6}$$

where $\boldsymbol{u}_{th}(t)$ is the analytical Womersley solution, $\boldsymbol{u}_{lb}(t)$ is the simulated velocity, and T is the number of time steps per period. For $\boldsymbol{u}_{th}$ we use the Womersley solution [14]. For flow in an infinite tube driven by pressure gradient $Ae^{i\omega t}$,

$$\boldsymbol{u}_{th} = \frac{AR^2}{\nu}\frac{1}{i^3\alpha^2}\left\{1 - \frac{J_0(\alpha i^{3/2}x)}{J_0(\alpha i^{3/2})}\right\}e^{i\omega t}, \tag{7}$$

where R is the radius of the tube, x is defined as $x=r/R$, $\omega = 2\pi/T$ is the circle frequency, J_0 is the zero-order Bessel function, and α is the Womersley number,

$$\alpha = \frac{D}{2}\sqrt{\frac{\omega}{\nu}}. \tag{8}$$

Here $D=2R$ is the diameter of the tube.

As an example, we show in Figs. 1 and 2 simulation results together with analytical solutions, for Re=10, $\alpha=6$ and Re=3000, $\alpha=16$, respectively. Other examples and more detailed comparisons can be found in [7,18,20].

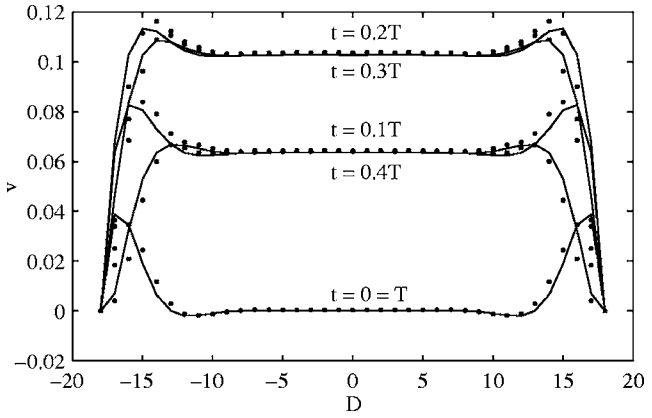

FIG. 2. Comparison of simulated velocity profile (dots) with analytical Womersley solution (solid line) for the tube with diameter $D=36$, Re=3000, $\alpha=16$.

The agreement in the case of low Re number is good while for Re=3000 the agreement is less good, especially near the walls. The simulation error in the first case is $\tilde{E}=0.002$, while for the second case it is $\tilde{E}=0.092$.

III. THE CONSTRAINT OPTIMIZATION SCHEME

A. General description

In LBM simulations for time harmonic flows one must specify four free parameters: the diameter D, the period T, the relaxation parameter τ (or related viscosity ν), and the Mach number Ma. The choice of these four parameters influences not only the accuracy of the method, but also other features like stability, convergence, and execution time. We will now address the question how to optimally choose these parameters. First we specify Re and α of the harmonic flow that we wish to simulate. With only these two constraints we have an undetermined system where we can freely choose two simulation parameters. In order to fix them, we apply the following rule. We specify a next constraint, the simulation error that we want to achieve, reducing the number of free parameters to 1. Finally, we demand that the remaining simulation parameter should be chosen such that the execution time is minimized. This still leaves us with many ways to select the simulation parameters that we use in the minimization procedure. We have chosen to take τ and Ma as the free parameters that will be fixed by the simulation error constraint and the execution time minimization constraint. These in turn determine the discretizations in time and space.

The Reynolds number Re is defined as

$$\mathrm{Re} = \frac{uD}{\nu} \tag{9}$$

and the Mach number Ma is

$$\mathrm{Ma} = \frac{|\boldsymbol{u}|}{c_s}. \tag{10}$$

Combining Eqs. (9) and (10) we get

$$D = \frac{\mathrm{Re}}{c_s}\frac{\nu}{\mathrm{Ma}}, \tag{11}$$

and combining Eqs. (8) and (11) results in

$$T = \frac{\pi\,\mathrm{Re}^2}{2c_s^2\alpha^2}\frac{\nu}{\mathrm{Ma}^2}. \tag{12}$$

Equations (11) and (12) express the spatial and temporal discretizations as a function of two constraints, and the remaining free parameters ν and Ma.

We need to realize that we have to enforce a minimum discretization D_{min} (to guarantee that the geometry is discretized at a minimum accuracy to capture the details of the flow) and a minimum required period T_{min} (due to the Nyquist sampling theorem stating the minimum number of sample points to represent a periodic signal). Due to these

minimum discretizations, we can enforce a few constraints on ν and Ma. Using Eqs. (11) and (12) we find

$$\nu \geqslant \frac{D_{min} c_s}{\mathrm{Re}} \mathrm{Ma} \tag{13}$$

and

$$\nu \geqslant \frac{2T_{min} c_s^2 \alpha^2}{\pi \mathrm{Re}^2} \mathrm{Ma}^2. \tag{14}$$

Moreover, for reasons of stability of LBM simulations (see Sec. IV) we must demand that $\nu \geqslant \nu_{min}$ (e.g., $\tau > \tau_{min}$) [21]. The minimum allowed viscosity, for small Ma, is then determined by this stability constraint. For larger Ma the minimum allowed viscosity is determined by the linear constrait of Eq. (13); for $\mathrm{Ma} > \mathrm{Ma}^*$ the minimum viscosity is determined by the quadratic constraint of Eq. (14). Here Ma^* is defined as the intersection between constraints (13) and (14),

$$\mathrm{Ma}^* = \frac{\pi D_{min} \mathrm{Re}}{2T_{min} c_s \alpha^2}. \tag{15}$$

Typically Ma^* is large, and we only need to worry about the linear constraint of Eq. (13). Our task is now to determine $\tilde{E}$ in the allowed simulation region, find contours of constant $\tilde{E}$, and minimize the execution time along those contours. One approach would be to measure $\tilde{E}$. Another is to study the asymptotic error behavior and try to obtain analytical expressions. We will follow both approaches.

B. Asymptotic error analysis

We assume three sources of error, those due to spatial and temporal discretization and due to the compressibility error. The errors due to spatial and temporal discretization are of first or second order, depending on the boundary conditions [18]. The compressibility error is known to be of second order in Ma [22,23]. We write the error as

$$\tilde{E} = \frac{k_x^{(n)}}{D^n} + \frac{k_t^{(n)}}{T^n} + k_m(\mathrm{Ma}^2) \tag{16}$$

where $k_x^{(n)}$, $k_t^{(n)}$, and k_m are coefficients that depend on details of the flow problem but do not depend on spatial or temporal discretization. n equals 1 or 2 depending on the boundary conditions (for BBCs $n=2$). By substituting Eqs. (11) and (12) into (16) and using Eq. (5) we find

$$\tilde{E} = \xi_x^{(n)} \frac{\mathrm{Ma}^n}{\left(\tau - \frac{1}{2}\right)^n} + \xi_t^{(n)} \frac{\mathrm{Ma}^{2n}}{\left(\tau - \frac{1}{2}\right)^n} + \xi_m(\mathrm{Ma}^2) \tag{17}$$

where $\xi_x^{(n)} = k_x^n c_s{}^n / \mathrm{Re}^n$, $\xi_t^{(n)} = k_t^n (2 c_s{}^2 \alpha^2)^n / (\pi \mathrm{Re}^2)^n$, and $\xi_m = k_m$. Next demand that $\tilde{E}$ has a constant value ε. From Eq. (17) we can now derive an isoerror contour for τ as a function of Ma and ε,

$$\tau = \mathrm{Ma} \left(\frac{\xi_x + \xi_t \mathrm{Ma}^2}{\varepsilon - \xi_m \mathrm{Ma}^2} \right)^{1/n} + \frac{1}{2}. \tag{18}$$

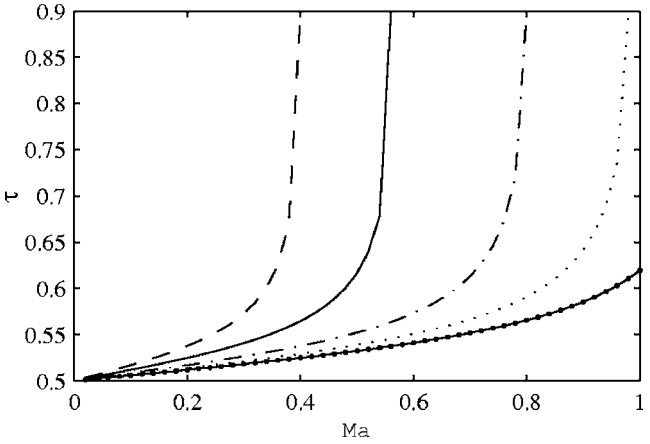

FIG. 3. Isoerror contours in the (Ma, τ) plane for Re=50 and $\alpha=6$ at $\tilde{E}=0.005$ (dashed), 0.01 (solid), 0.02 (dot-dashed), 0.03 (dotted), and 0.04 (barred).

The execution time T_{exec} for the LBM for time harmonic flows can be written as

$$T_{exec} = N_p T_p, \tag{19}$$

where N_p is the number of periods that are needed to achieve a stable time harmonic solution and $T_p = T t_{iter}$ is the execution time per period, with t_{iter} the execution time for one LBM iteration. Finally, $t_{iter} = D^3 t_{node}$, where t_{node} is the time spent to update one node in the lattice. For our simulations we assume that we have D^3 nodes. From previous experiments [18] we know that N_p hardly depends on other parameters and for our case we assume that it is constant. Thus Eq. (19) can be written as

$$T_{exec} = N_p T D^3 t_{node} = C_t T D^3, \tag{20}$$

where C_t is a constant. If we substitute Eqs. (11) and (12) into (20) and invoke Eq. (18) we get

$$T_{exec} = C_t \frac{\pi \mathrm{Re}^5}{2 c_s{}^5 \alpha^2} \frac{1}{\mathrm{Ma}} \left(\frac{\xi_x + \xi_t \mathrm{Ma}^2}{\varepsilon - \xi_m \mathrm{Ma}^2} \right)^{4/n}. \tag{21}$$

Independent of n, T_{exec} goes to infinity for Ma decreasing to 0 [because T then goes to infinity; see Eq. (12)] and for Ma reaching the value $\sqrt{\varepsilon / \xi_m}$ [because ν and therefore D go to infinity; see Eqs. (11) and (18)] T_{exec} has a minimum between these two limiting values. Later we will compare our experimental results to these analytical solutions. Plots of the asymptotic isoerror contours are shown in Fig. 3. Here we assumed $k_x = k_t = 1$ and $k_m = 0.05$, and second-order boundary conditions, i.e., $n=2$.

Using Eq. (20) we have plotted in Fig. 4 $\ln(T_{exec}/C_t)$ as a function of Ma along the analytical isoerror curves. Each of the contours has a minimum point which corresponds to the optimal value of Ma for a certain $\tilde{E}$. For example, for $\tilde{E} = 0.005$, T_{exec} has its minimum at Ma=0.18 and as Ma increases toward $\sqrt{\varepsilon / \xi_m}$, T_{exec} grows to infinity.

C. Experimental results

We performed three sets of experiments: Re=50, $\alpha=6$, Re=200, $\alpha=6$, and Re=1200, $\alpha=16$. We measured the error

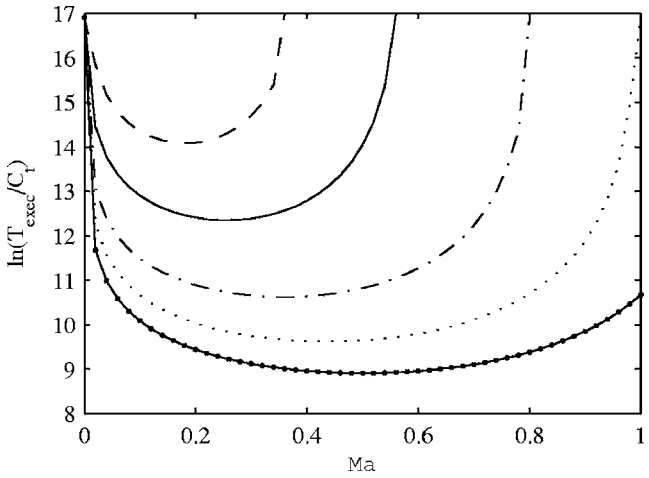

FIG. 4. $\ln(T_{exec}/C_t)$ as a function of Ma along isoerror contours for Re=50 and $\alpha=6$ at $\tilde{E}=0.005$ (dashed), 0.01 (solid), 0.02 (dot-dashed), 0.03 (dotted), and 0.04 (barred).

on every time step for a range of values of Ma and τ and from that we compute the average error $\tilde{E}$ and its standard deviation. In Table I the standard deviations for $\tilde{E}=0.0032$, 0.0054, and 0.009 are shown. Note that $\tilde{E}$ is measured at each time step and averaged over the period.

Figure 5 shows the experimental isoerror curves (markers) for Re=50, $\alpha=6$. These experimental results suggest that the Ma-τ correlation is linear. In the limit of small Ma Eq. (18) can be written as

$$\tau = \left(\frac{\xi_x}{\varepsilon}\right)^{1/n} \mathrm{Ma} + \frac{1}{2}. \tag{22}$$

Fitting the experimental data with Eq. (22) results in a different coefficient k_x for each $\tilde{E}$. To improve this, we fit the experimental data with the analytical isoerror curves (solid lines) for the complete Eq. (18) for $n=2$. We find a very good agreement between experimental and analytical results. Now the values of k_x, k_t, and k_m are the same for all $\tilde{E}$. The same fitting has been done for Re=200, $\alpha=6$ and Re=1200, $\alpha=16$. In Table II we show the resulting values of the k_x, k_t, and k_m coefficients. In order to evaluate the influence of the spatial, temporal, and compressibility errors on the simulation results we fit the obtained data shown in Table II into Eq. (16). The magnitudes of D and T when Re=50, $\alpha=6$, and Ma=0.2 are 38 and 650, respectively, for $\tilde{E}=0.0032$. We substitute these parameters into Eq. (16) and observe that $\tilde{E}$ is mostly caused by the spatial discretization and the influence of the compressibility error is almost unnoticeable (data not shown). This agrees with the result of Shi *et al.* [24] that the simulation error is almost not influenced by compressibility error. The results confirm the second-order behavior in time and space as demonstrated in [12,20]. The values of k_m in the Table II are quite small and are the threshold ones; for higher values the fitting breaks down and for smaller ones it does not improve. We measured the standard deviation of the fitting error and for this specific case they are small, e.g., for space discretization it is of magnitude 0.006. This shows that we got a good agreement between analytical and experimental results.

TABLE I. Standard deviation for several $\tilde{E}$'s.

Re	α	Ma	τ	$\tilde{E}$	Deviation
50	6	0.2	0.7	3.2×10^{-3}	2×10^{-4}
200	6	0.4	0.9	5.4×10^{-3}	4×10^{-4}
1200	16	0.2	0.7	9×10^{-3}	7×10^{-4}

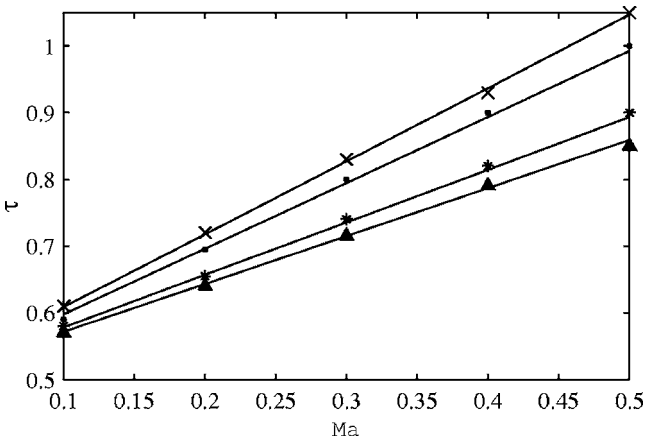

FIG. 5. Isoerror contours in the (Ma, τ) plane of both analytical and experimental errors $\tilde{E}=0.0026$ (×), 0.0032 (●), 0.005 (∗), and 0.006 (▲) for a range of τ and Ma, for Re=50 and $\alpha=6$.

We compared the analytical and experimental results of T_{exec} in Fig. 6. The analytical curves are obtained from Eq. (21), where $C_t=40t_{node}$. t_{node} is the time spent to update one node in the lattice and in our case is 2×10^{-7} s.

Note that even for very large Ma numbers we accurately reproduce the theoretical Womersley solutions. When inspecting the results as a function of time, the velocity in the tube is close to the theory for both and small and large Ma numbers. This is surprising, as we always assume that Ma $\ll 1$ in order to suppress compressibility errors. We believe that our benchmark, a straight three-dimensional (3D) tube, may be too simple and allows for such large Ma without deteriorating the results. As is well known, a time-independent 2D Poisseulle flow is an exact solution of the lattice Boltzmann equations [25]. If the boundary conditions are chosen in a correct way, the LBM will be exact in that case for any Ma number. We expect, but did not check this explicitly, that this may also hold for time harmonic 2D

TABLE II. The values of spatial k_x, temporal k_t, and compressibility error k_m coefficients for Re=50, 200, 1200 and correspondingly $\alpha=6$, 6, 16.

Case	k_x	k_t	k_m
Re=50, $\alpha=6$	4.8	1.9	<0.0001
Re=200, $\alpha=6$	20	10	<0.001
Re=1200, $\alpha=16$	240	120	<0.01

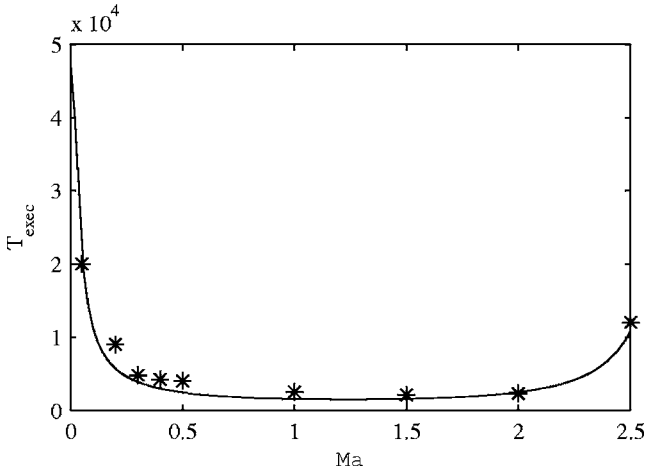

FIG. 6. Comparison of T_{exec} as a function of Ma for Re=50, α=6 for $\tilde{E}$=0.0032 (∗) with the analytical T_{exec} (solid line).

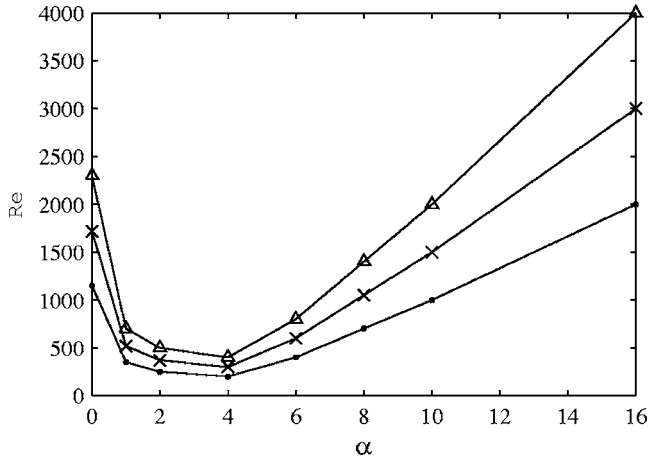

FIG. 7. Threshold values of Reynolds number for a certain range of Womersley numbers for u_{max}=0.1, D=24 (●), 36 (×), and 48 (△). The stability regions are below the lines.

Womersley flow, and that the results can be carried over to three dimensions. However, in three dimensions the symmetry is slightly broken due to the discretization of the tube. Due to our constraints, a large Ma means an extremely fine spatial discretization [see Eq. (11)]. This may be the reason that we are able to run our simulations quite accurately for such large Ma. When going to realistic geometries, like the aorta in Sec. V, we expect that we must keep the Mach number at more familiar values, i.e., less than 1.

Both plots in Fig. 6 have similar behavior, that is, for a specific parameter set there exists a minimum T_{exec}. One should be aware of this behavior in order to chose optimal simulation parameters with minimum T_{exec} under the given constraints.

As a conclusion we confirm that by using the constraint optimization scheme it is possible to find a parameter set that gives the minimum T_{exec} for desired $\tilde{E}$. Also in our asymptotic error analysis we have shown the second-order behavior of $\tilde{E}$. From detailed comparisons of experimental and analytical results we showed that the Ma-τ correlation is linear and observed that the error is not influenced by compressibility error. This may be due to the complete symmetry of the geometry, as for real cases we expect to see an essential influence of compressibility error.

IV. STABILITY OF TIME HARMONIC LBM SIMULATIONS

The numerical stability of the LBM has been studied by many authors, e.g., [21,26–28]. These studies are mainly performed assuming uniform, time-independent background flow. The stability of the LBM depends on three conditions [21]. First, the relaxation time τ must be $\geqslant$0.5 corresponding to positive shear viscosity. Second, the mean flow velocity must be below a maximum stable velocity; and third, as τ increases from 0.5, the maximum stable velocity increases monotonically until some fixed velocity is reached, which does not change for larger τ.

In our experiments we fix Ma (u=0.1) and for a range of α we push Re to its highest possible values by decreasing ν. Divergence of the momentum profiles is considered to be a definite sign of instability in the system. In order to have a large range of Re number we chose three different cases D =24, 36, and 48.

In Fig. 7 the highest attained Re numbers as a function of α are plotted. We observe the growth of the stability limit for Re with increasing α. As we can see from the plots the maximum Re we reached for static flows is 2300 for D=48. This indicates that the system is still stable for τ=0.506 and u=0.1. This is comparable to the 2D results obtained by Lallemand and Luo [26].

The threshold values of Re for time-dependent flows are much higher, e.g., Re=4000 for D=48 at α=16.

It is known that the transition into turbulence appears at high Re numbers. The transition starts at $\mathrm{Re}_\delta \sim 850$, where Re_δ is the Reynolds number based on the Stokes layer thickness [29]. Moreover, experimental results of Shemer [30] indicate that the threshold value of transition into turbulence in a slowly pulsating pipe flow is Re=4000. These results confirm that we observe numerical instabilities in this laminar regime.

In the graph for larger values of α we see almost linear behavior. The interesting part is when the value of α is $\leqslant$6 while the viscous forces are dominating. Here the limiting magnitude of Re can be quite small.

With these measurements we confirm that for time harmonic flows it is possible to reach high Re numbers especially with second-order wall boundary conditions. From our experiments we observe that when bounce back on links (BBL) boundary conditions were used the system is less stable, especially for small α=2,3 for Re=10.

In order to compare the minimum τ for all D=24, 36, and 48 cases, in Fig. 8 we plot the minimum ν as a function of $D^2\omega$. We see a complete overlap of obtained profiles, which implies that the stability depends on the magnitude of $D^2\omega$.

We also note that the obtained large Re numbers are possible only for the idealized tube. For real cases (see Sec. V) it is already difficult to reach stability for small Re numbers. In future work we will extend and investigate in more detail

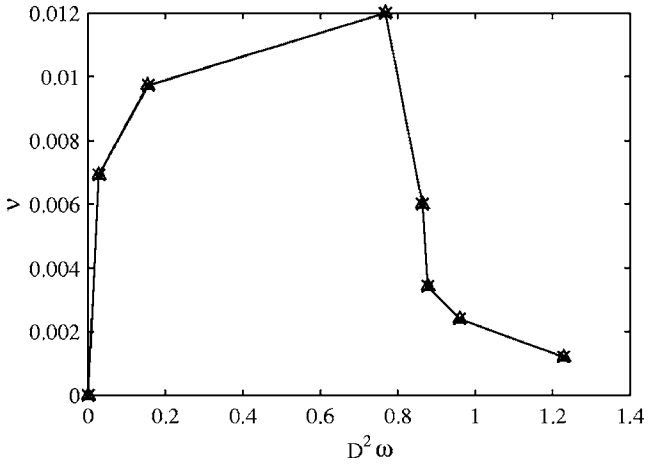

FIG. 8. The minimum ν as a function of $D^2\omega$ for the given range of Reynolds and Womersley numbers for $u_{max}=0.1$, $D=24$ (●), 36 (×) and 48 (△).

all these observations. Currently we do not have a good explanation for the behavior we observed in Fig. 8.

V. HARMONIC FLOW IN HUMAN ABDOMINAL AORTA

We applied a constraint optimization scheme in the simulation of harmonic blood flow in the lower abdominal aorta [6]. The two constraints, Re=600 and $\alpha=4$, are typical values in the lower abdominal aorta of a person in resting condition [31]. For this simulation we used first-order boundary conditions on the walls and time harmonic pressure difference on inlet and outlet layers. We performed the experiments of a constraint optimization scheme for BBL boundary conditions (as in Sec. IV, data not shown). We used the resulting values for the simulation of blood flow in the lower abdominal aorta. The errors associated with this boundary condition are at least three times higher than in the case of BBCs [18]. For the given Re and α constraints we had to choose Ma=0.1 in order to keep $\tilde{E}=10\%$ while minimizing the execution time. Here the relaxation parameter $\tau=0.514$. The characteristics of observed flow fields together with backflows above the bifurcations are in a good agreement with the results obtained in [6,31]. In Fig. 9 we show one case of our observations near the main bifurcation.

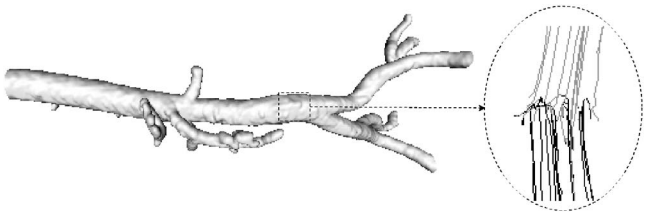

FIG. 9. Lower abdominal aorta for Re=600 and $\alpha=4$. Velocity profile shown by streamlines (black, backflows, gray forward flows).

VI. CONCLUSIONS

In this paper we have presented results of simulation of time harmonic flows with the LBM. We have defined a constraint optimization scheme and proved that using this scheme it is possible to find a parameter set that gives the minimum execution time for a predefined simulation error. We performed both an asymptotic error analysis and experimental measurements. We conclude that the simulation error is hardly influenced by compressibility error. From stability measurements of the system, we found a unique dependence of the minimum allowed viscosity as a function of $D^2\omega$. This needs further study. Finally, we applied the constraint optimization scheme on our simulations of blood flow in the lower abdominal aorta. We performed examinations of flow profiles and showed qualitative agreement with the experimental results.

ACKNOWLEDGMENTS

The work was funded by the Dutch National Science Foundation, NWO, through the Token 2000 Distributed Interactive Medical Exploratory for 3D Medical Images (DIME) Project No. 634.000.024. We acknowledge Dominique d'Humieres for helpful discussions.

[1] S. Succi, *The Lattice Boltzmann Equation for Fluid Dynamics and Beyond* (Oxford University Press, New York, 2001).
[2] Sh. Chen and G. D. Doolen, Annu. Rev. Fluid Mech. **30**, 329 (1998).
[3] A. Koponen, D. Kandhai, M. Kataja, and J. Timonen, Int. J. Mod. Phys. C **9**, 1505 (1998).
[4] D. S. Clague, B. D. Kandhai, R. Zhang, and P. M. A. Sloot, Phys. Rev. E **61**, 616 (2000).
[5] D. Kandhai, D. Hlushkou, A. G. Hoekstra, P. M. A. Sloot, H. Van As, and U. Tallarek, Phys. Rev. Lett. **88**, 234501 (2002).
[6] A. M. Artoli, A. G. Hoekstra, and P. M. A. Sloot, J. Biomech. **39**, 873 (2005).
[7] A. M. Artoli, A. G. Hoekstra, and P. M. A. Sloot, Int. J. Mod. Phys. B **17**, 95 (2003).
[8] J. A. Cosgrove, J. M. Buick, S. J. Tonge, C. G. Munro, C. A. Greated, and D. M. Campbell, J. Phys. A **36**, 2609 (2003).
[9] Zh. Guo, Ch. Zheng, and T. S. Zhao, J. Sci. Comput. **16**, 569 (2001).
[10] H. Fang, Z. Wang, Z. Lin, and M. Liu, Phys. Rev. E **65**, 051925 (2002).
[11] Zh. Guo, T. S. Zhao, and Y. Shi, Phys. Rev. E **70**, 066706 (2004).
[12] D. Kandhai, A. Koponen, A. G. Hoekstra, M. Kataja, J. Timonen and P. M. A. Sloot, J. Comput. Phys. **150**, 482 (1999).
[13] J. Toelke, M. Krafczyk, and E. Rank, J. Stat. Phys. **107**, 573 (2002).
[14] J. R. Womersley, Philos. Mag. **46**, 199 (1955).
[15] S. Chen, Z. Wang, X. Shan, and G. Doolen, J. Stat. Phys. **68**,

379 (1992).
[16] Y. H. Qian, D. d'Humieres, and P. Lallemand, Europhys. Lett. **17**, 479 (1992).
[17] M. Bouzidi, M. Firdaouss, and P. Lallemand, Phys. Fluids **13**, 3452 (2001).
[18] A. M. Artoli, A. G. Hoekstra, and P. M. A. Sloot, Comput. Fluids **35**, 227 (2005).
[19] D. Kandhai, A. Koponen, A. G. Hoekstra, M. Kataja, J. Timonen, and P. M. A. Sloot, Comput. Phys. Commun. **111**, 14 (1998).
[20] A. M. Artoli, A. G. Hoekstra, and P. M. A. Sloot, Int. J. Mod. Phys. C **13**, 1119 (2002).
[21] J. D. Sterling and S. Chen, J. Comput. Phys. **123**, 196 (1996).
[22] G. Hazi, Phys. Rev. E **67**, 056705 (2003).
[23] D. O. Martinez, W. H. Matthaeus, and S. Chen, Phys. Fluids **6**, 1285 (1993).
[24] Y. Shi, T. S. Zhao, and Z. L. Guo, Phys. Rev. E **73**, 026704 (2006).
[25] X. He and L.-S. Luo, J. Stat. Phys. **88**, 927 (1997).
[26] P. Lallemand and L.-S. Luo, Phys. Rev. E **61**, 6546 (2000).
[27] X. D. Niu, C. Shu, Y. T. Chew, and T. G. Wang, J. Stat. Phys. **117**, 665 (2004).
[28] R. A. Worthing, J. Mozer, and G. Seeley, Phys. Rev. E **56**, 2243 (1997).
[29] J. A. Crosgrove, J. M. Buick, S. J. Tonge, C. G. Munro, C. A. Greated, and D. M. Campbell, J. Phys. A **36**, 2609 (2003).
[30] L. A. Shemer, Phys. Fluids **28**, 3506 (1985).
[31] Ch. Taylor, T. J. R. Hughes, and Ch. K. Zarins, Comput. Methods Appl. Mech. Eng. **158**, 155 (1998).